ELSEVIER

Contents lists available at ScienceDirect

# Journal of Cleaner Production

journal homepage: www.elsevier.com/locate/jclepro





# Towards building homeostasis through a low-cost biomimetic synthetic foam for building surface cooling and energy saving

Yawen He<sup>a</sup>, Adam Brooks<sup>a,b</sup>, Yucen Li<sup>a</sup>, Hongyu Zhou<sup>a,\*</sup>

- a Department of Civil and Environmental Engineering, University of Tennessee, Knoxville, TN, USA
- <sup>b</sup> Nuclear Energy and Fuel Cycle Division, Oak Ridge National Laboratory, Oak Ridge, TN, USA

# ARTICLE INFO

Handling Editor: Zhen Leng

Keywords: Biomimetic material Microstructure Evaporative cooling Building energy

#### ABSTRACT

Evaporative cooling has been demonstrated as one of the most effective means to reduce a building's energy consumption and achieve homeostasis in buildings without intensive energy demands. In this research, a novel biomimetic inorganic synthetic foam material (BMSF) was developed from reclaimed fly ash cenospheres for building surface cooling. The BMSF material is synthesized from an abundant industrial byproduct (i.e., fly ash cenosphere) through a low-cost and high-yield two-step process. X-ray microtopography (XRM) and scanning electron microscopy (SEM) tests revealed that BMSF has a microstructure that resembles that of the keratinous skin of African elephants and certain desert lizards to enable water to be stored and transported effectively through capillary actions. Experiments were carried out to quantify the evaporative behavior and cooling effect of the material and building roofs equipped with the BMSF panels. The experimental results indicate remarkable cooling performance – i.e., BMSF panels with protruded surfaces have higher evaporation rates than that of open water surface and a surface temperature reduction of 15 °C–25 °C was achieved. Lastly, case studies were carried out on a single-story commercial building in Los Angeles, California, and the results demonstrate that the new evaporative cooling surface material is able to achieve passive cooling for buildings in areas with a mild climate and low relative humidity.

### 1. Introduction

The International Energy Agency (IEA) estimates that the building sector accounts for 40% of total energy consumption worldwide (Xu and Dessel, 2008), where a substantial portion is attributed to the operational energy used for space heating/cooling and ventilation. Passive cooling is one of the most effective means to achieve the energy-saving targets of net-zero energy buildings (Net ZEB) (Athienitis and Brien, 2015). Passive techniques can meet indoor thermal comfort requirements with low energy consumption. Due to its direct exposure to solar radiation, the building roof alone can be responsible for up to about 50% of the thermal load in single or two-story buildings (Nahar et al., 2003). Therefore, regulating heat gain of building roofs through passive cooling techniques is of interest to both academia and industry. In the past two decades, different evaporative cooling techniques, such as roof shading (Kumar and Kaushik, 2005), increasing the insulation and thickness (thermal mass) (Al-Sanea et al., 2012), roof vegetating (Shafique et al., 2018), roof spray (ketanHagishima and Tanimoto, 2020), and roof ponds (Sharifi and Yamagata, 2015), have been

explored. However, most of the techniques developed so far require the installation of complicated plumbing (pump) systems or the use of non-durable surface materials such as hydrogel (Rotzetter et al., 2012), which would inevitably increase the maintenance costs of building roof systems and may cause issues like water leakage (roof ponds) and microbial growth. Moreover, few existing approaches to date simultaneously have the properties of high cooling efficiency, long durability (e. g. resistance to thermal cycling and UV irradiation), and low cost (Cuce and Riffat, 2016).

In nature, plants and animals are autonomously adaptive to the changing ambient environment (e.g., temperature, relative humidity) through transpiration and perspiration of water, which has one of the highest latent heats among various fluids. Inspired by the passive biological cooling process, several self-adaptive cooling technologies related to bio-inspired artificial skins have been reported, including superabsorbent polymer (i.e., hydrogel) based building skin (Cui et al., 2016), and thermochromic reflective coatings (Berardi et al., 2020). In comparison with inorganic materials, hydrogels are generally less durable and are susceptible to UV deterioration and wet-dry cycling, which may hinder their long-term application as building surfaces. The

<sup>\*</sup> Corresponding author. 851 Neyland Drive,417 John D. Tickle Building, Knoxville, TN, 37996-2313, USA. *E-mail address:* hzhou8@utk.edu (H. Zhou).

Nomenclature		WWR	Window-to-wall ratio [—]
$A$ $c_p$ $F$ $h_c$ $h_m$ $H$ $I_s^1$ $J$ $Le$ $LE$ $LPD$ $m$ $PMV$ $PPD$ $Q$ $SHGC$ $t$ $T$ $u$ $U$ $v_{ex}$ $V$ $W$	Area [m²]  Specific heat [J/(kg·K)]  View factor [—]  Surface heat transfer coefficient [m/s]  Surface mass transfer coefficient [m/s]  Heat transfer coefficient [W/K]  Solar radiation incident [W/m²]  Diffusive mass flux [kg/m²]  Lewis number [—]  Energy flux [W/m²]  Long-term Percentage of Dissatisfied [%]  Mass [kg]  Predicted mean vote [—]  Predicted percentage of dissatisfied [%]  Heat transfer rate [W]  Solar heat gain coefficient [—]  Time [s]  Temperature [°C]  Moisture content [kg/m³]  Thermal transmittance [W/(m²·K)]  Air velocity [m/s]  Differential control volume or finite control volume [m³]  Water mass [kg]	Greek sy $\alpha$ $\varepsilon$ $\lambda$ $\rho$ $\sigma$ $\tau$ Subscrip $a$ $abs$ $air_ex$ $b$ $c$ $grd$ $lat$ $lw$ $sat$ $sky$ $sw$ $v$	Solar absorptance [—] Surface emissivity [—] Wavelength [nm] Density [kg/m³] Stephan-Boltzmann constant [W/(m²·K⁴)] Reflectance [—]  Its and superscripts Air Thermodynamic temperature Outdoor air Biomimetic mesoporous synthetic foam layer Concrete Ground (long-wave radiation) Latent heat Long-wave radiation Saturated state Sky (long-wave radiation) Short-wave radiation vapor Wall layer

remarkable cooling ability of certain animal skins like the ones of the African elephant (Loxodonta) stems from the morphology-enabled moisture absorption and evaporative cooling. Inspired by its hierarchical functional structures, a biomimetic 'hydro-foam', namely biomimetic mesoporous synthetic foam (or BMSF), is developed herein as an evaporative cooling layer for building roofs. The microstructure of the evaporative layer was inspired by the morphological features of certain animal skin driving the water transport and storage to enable evaporative cooling on elephant skin surfaces. The mesoporous synthetic foam is formed by a 'minimal-contact' process developed by the authors (Zhou and Brooks, 2019; Brooks et al., 2018), where micro-size fly-ash cenospheres (FACs) are bonded through drying a clay-water suspension before it is sintered into an inorganic synthetic foam with over 95% interconnected pores. Thus, the foam layer can be effectively used to store rainwater (Wanphen and Nagano, 2009; Zhang et al., 2018) and roof run-offs for prolonged evaporative cooling. The material developed herein also has other advantages such as being lightweight and low-cost as compared to superabsorbent polymers and traditional porous materials used for roof cooling (Wanphen and Nagano, 2009; Karamanis, 2015; Shokri Kuehni et al., 2016). In addition, since the material is made from sintered inorganic minerals, it is not susceptible to UV-induced degradation. The evaporation rate from the BMSF flat panel was tested very close to that of an open water surface, leading to a high cooling effect for AC load reduction. In addition, surface topology such as protruded surfaces can be effective at increasing the surface area, which leads to even higher evaporation rates from BMSF than that of an open water surface. The BMSF surfaces can also be easily extended to the application for vertical building surfaces, which have the potential to significantly reduce the energy consumption of mid- and high-rise buildings. The evaporative cooling performance of the BMSF layer is validated through experimental studies for concrete roofs under different scenarios. Moreover, a thermal network model was developed to quantify the energy-saving potential and thermal comfort performance of the biomimetic mesoporous synthetic foam (BMSF) for a case study building located in Los Angeles, California.

# 2. Material and methods

# 2.1. Biomimetic inorganic synthetic foam manufactured from reclaimed fly-ash

Typically, animals with large bodies tend to retain more heat due to their relatively small ratio of surface area to body volume for heat dissipation. Elephants, for example, with their heavyweight frames, would appear to be at a disadvantage in the fierce heat of their African and Asian habitats, especially because they lack sweat glands. Recent studies discovered that an intricate network of crevices adorns the skin surface of the African bush elephant. These micrometer-wide channels enhance the effectiveness of thermal regulation (by water retention), as well as protection against parasites and intense solar radiation (Martins et al., 2018).

To mimic the water transport, evaporation, and storage behavior found in animal skins, in this research a mesoporous inorganic synthetic foam was developed using an industrial byproduct - fly ash cenospheres (FAC). FAC are hollow aluminosilicate microspheres that are produced as a byproduct during the coal combustion process. It is featured by low bulk density (400 kg/m<sup>3</sup>–900 kg/m<sup>3</sup>) and is nearly spherical in shape with highly selectable particle size distributions - from several micrometers to several hundreds of micrometers in diameter (Zhou and Brooks, 2019; Brooks et al., 2018). In addition, FAC surfaces are mostly hydrophilic and have large interior cavity spaces (over 80% by volume) for water storage if needed. The hydrophilic surface of FAC also promotes wicking and capillary water transport within the BMSF material, which helps water to evenly distribute across the entire evaporation surface (Zhou et al., 2017). These features make FAC an ideal material to produce low-cost inorganic synthetic foam, which resembles the keratinous skin of African elephants, see Fig. 1.

To prepare the synthetic solid foam, a clay-water mixture was prepared as the binder for the FAC skeleton. First, the binding clay was mixed with water into a slurry. The FACs were then mixed with the clay slurry to form a composite paste, see Fig. 1 (a). The composite paste was

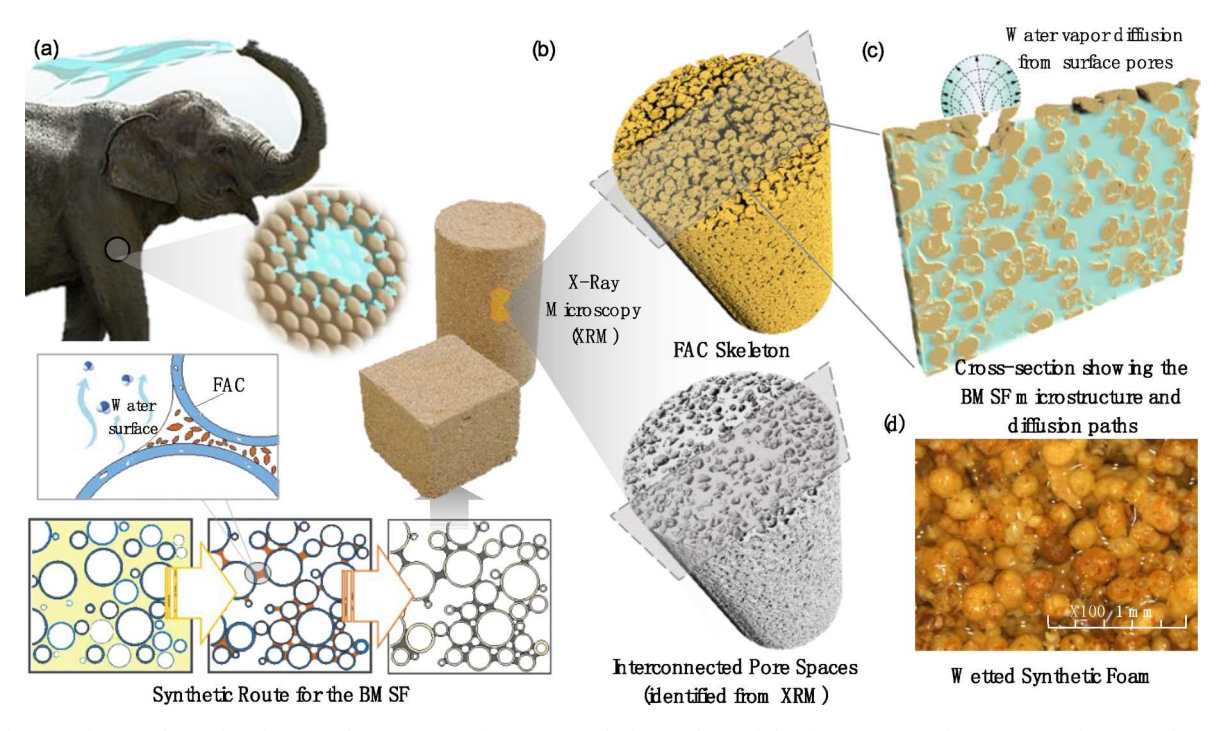


Fig. 1. Schematic showing the analogy between the evaporation from African elephants' skin and that from BMSF (a) the wetting mechanism and manufacturing process; (b) microstructure tested by XRM; (c) inter-particle pore structure; and (d) optical micro-image showing the wetted BMSF.

dried in a convection oven. During the drying process, the capillary effect (surface tension between water and the FAC surfaces) causes clay particles to precipitate at the locations where the FACs are in contact (with some smaller amounts precipitated on the FAC surfaces). After drying, the material is sintered at 1050 °C to vitrify the clay particles into a contiguous, amorphous glassy solid, which acts as bridges to bind the FAC skeleton into a monolithic porous material. Details of the process to make the inorganic synthetic foam can be found in the authors' earlier publications (Zhou and Brooks, 2019; Brooks et al., 2018). For this research, a larger particle-size FAC (ES200/600 with the average particle size of 350 µm) was selected. To prepare 1 m<sup>3</sup> wet paste, 137.1 kg moist clay (~40% water content), 378.3 kg FAC, and was used and 105 kg additional water. The fired density of the BMSF was tested at 479.1 kg/m<sup>3</sup>. There is minimal overall volume change from the wet paste to the sintered synthetic foam. It is noted that current standard building brick is fired between 900 °C and 1300 °C for 10 hours-40 hours depending on the type of kiln used, and the manufacturing of proposed BMSF can be fully integrated into the existing brick-making systems; however, due to the porous nature of BMSF and its smaller thermal mass, it is believed that the firing time could be significantly reduced. However, no test was performed to find the optimal firing condition during the current work. The reduction in firing duration leads to less energy required for the production of the BMSF bricks when compared to standard building bricks (Brick Industry Association, 2006). The BMSF produced has a high volume of interconnected void space that can be utilized for water storage and a microstructure that facilitates the transport and evaporation of water for building surface cooling. As for material cost, the current price for fly ash cenospheres is \$389/ton-\$1289/ton (or \$0.38/kg-\$1.29/kg), for a 1-inch (25.4-cm) thick cladding panel or roof paver, the material cost is estimated at 0.4-1.25 per square foot (0.0929 m<sup>2</sup>). Considering the production (which is very similar to that of fired brick production) and transportation cost, the final BMSF cost (materials only) is estimated at \$1.5-\$4 per square foot ( $/0.0929 \text{ m}^2$ ), which is comparable to the brick veneer cost in the US (\$2-\$6 per square foot (/0.0929 m<sup>2</sup>) (Grupa, 2022)). The material is mechanically strong with tunable mechanical properties as demonstrated in the authors' previous publication (Brooks

et al., 2020). Due to the gradual shortage of fly ash (and thus FAC), alternative materials for making BMSF may include pumice, zeolite, or expanded shale/clay; however, testing of these materials lies outside the scope of the current work.

# 2.2. Microstructure

Fig. 2 (a) shows the microstructure of the BMSF reconstructed from the X-ray microtopography (XRM) data (Carl Zeiss Versa 520). The raw XRM data was processed and reconstructed using ORS Dragonfly. The capillary pore structure formed by the FAC skeleton is presented in Fig. 2 (b) with the total porosity of 68.7%. The connected interparticle pore spaces can facilitate fast water absorption through capillary wicking. In addition, the microstructure of BMSF also possesses a large number of 'closed' pore space formed by the hollow FAC (see Fig. 2 (b)) – note that these 'closed' pore space can slowly absorb and desorb water through the small pores within FAC shell. This is verified through geometric parameter characterization conducted using DragonFly which shows that the interconnected pore occupies 99.1% of the whole pore space. The pore-size distribution of these 'closed' pore spaces was analyzed using DragonFly and is presented in Fig. 2 (c). As a result, during rainy days, water can be stored within the cavity spaces in FAC and released later while evaporation takes place, see Fig. 2 (d). In addition, during the evaporation process, a water film forms on the hydrophilic FAC particle surface which will further increase the evaporation rate (Prat, 2007). As a result, a high evaporation rate (nearly identical to that of open water surfaces) was observed for saturated BMSFs. The high evaporation rate contributes to improved cooling efficiency, which could be critical for thermal load reduction for buildings.

# 2.3. Characterization of evaporation and drying behavior of BMSF

# 2.3.1. Evaporation rate and drying behavior

In order to characterize the water evaporation behavior of BMSF, drying tests were conducted on the material under different temperatures and relative humidity (RH) levels. Evaporation from porous media is a highly dynamic process that may vary considerably in space and

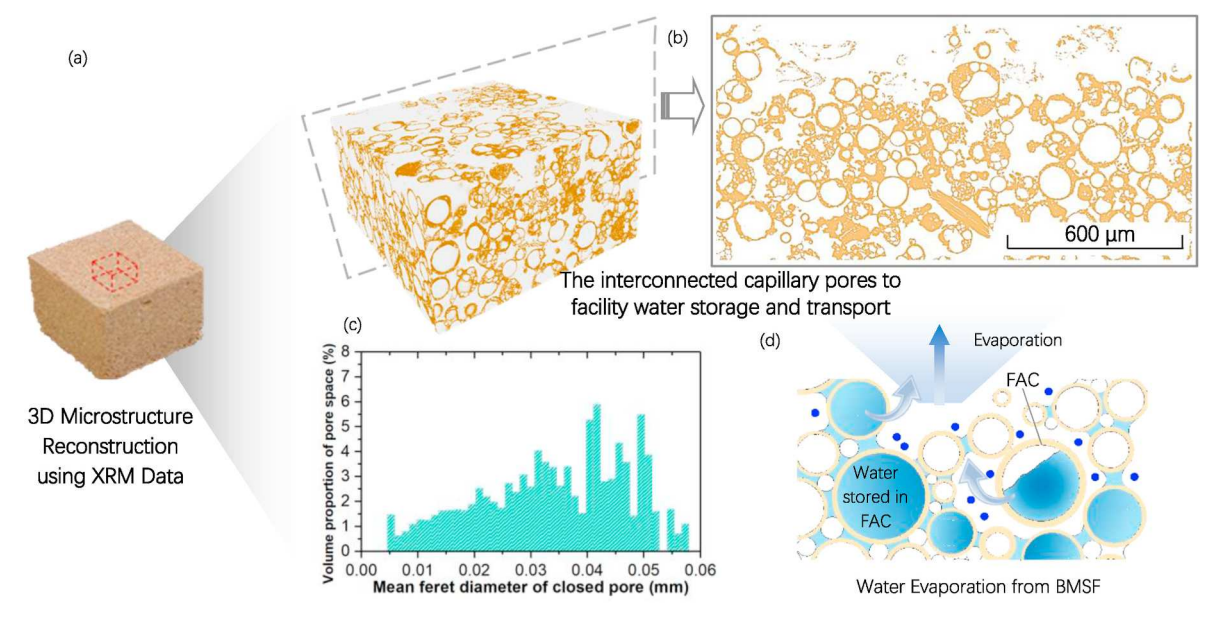


Fig. 2. Microstructure of the BMSF: (a) the FAC skeleton and interconnected pore network reconstructed from 3D X-ray Microtopography (XRM) data; (b) CT images showing the microstructure; and (c) pore size distribution of closed pores corresponding to volume proportion of closed pore space within the BMSF (d) perceived evaporation mechanism.

time reflecting the interplay between internal flow processes (i.e., capillary liquid flow to vaporization surface and vapor diffusion) and atmospheric conditions (e.g., energy input, air temperature, and relative humidity) (Shahraeeni et al., 2012; Haghighi and Or, 2013; Kumar and Arakeri, 2019; Adán et al., 2019; Mosthaf and HelmigDO, 2014; Shahraeeni and Or, 2012). The evaporation from porous media is typically conceptualized with two distinct stages: during Stage-1 evaporation (when the water content within the porous media is relatively high), liquid menisci in fine pores at the surface remain coupled with the atmosphere (as long as menisci curvature does not exceed pore critical invasion pressure). These hydraulically connected evaporating pores support a capillary gradient and draw water from the porous medium interior to supply evaporative demand at the surface, see Fig. 3. When the material loses constant water supply and as surface evaporation continues, the hydraulic continuity at the drying front surface is disrupted. Subsequently, liquid menisci recede from the surface to a level

below the surface and form a new vaporization plane referred to as the secondary drying front (Shokri and Or, 2011). This transition marks the onset of Stage-2 evaporation, where the material undergoes a lower evaporation rate limited by diffusion through the porous media.

During Stage-1 evaporation, the evaporation rate from the saturated surface of the porous foam is similar to the scenario of evaporation from an open water surface. The evaporation rate  $J_{\nu}$  per unit area under the saturated state (stage one) can be expressed as (Poós and Varju, 2020):

$$J_{v} = h_{m}[u_{v} - u_{a}] \tag{1}$$

where  $h_m$  is surface mass transfer coefficient;  $u_v$  is moisture content of material surface;  $u_a$  is moisture content of bulk air. During Stage-2 evaporation (see Fig. 3 (a)), the mass transfer is dominated by diffusion through the porous foam media. Therefore, evaporation can be depicted by mean vapor mass flux through the foam via mass transfer resistance, where the mass transfer is dominated by effective surface

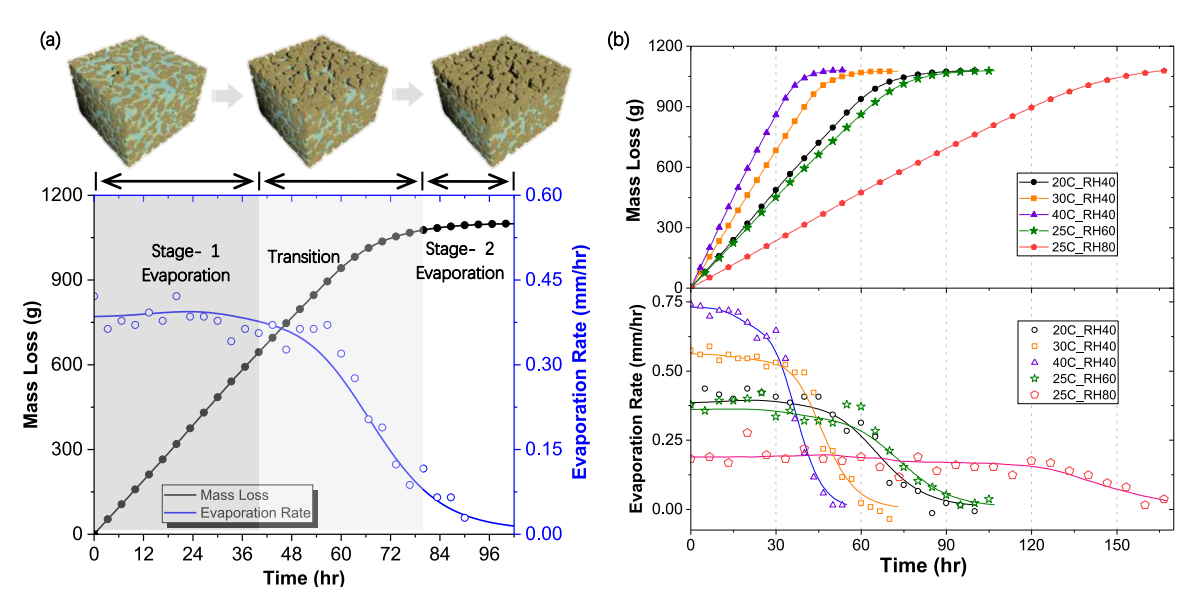


Fig. 3. Evaporation behavior of BMSF: (a)two-stage evaporation from the BMSF; (b) mass loss and evaporation rate of BMSF under different conditions.

#### resistance (Thomas and DMB, 1990).

To quantify the surface mass transfer property of the BMSF material, evaporation tests were performed under various temperature and relative humidity (RH) combinations, and the results (i.e., mass loss and evaporation rate) are plotted in Fig. 3 (b). The data measured by the digital balance were used to calculate the cumulative mass loss and the evaporation rate, as shown in Fig. 3 (b). During the experiments, ambient temperature and relative humidity were controlled by an environmental chamber. As mentioned earlier, Stage-1 evaporation is controlled by external conditions since the material is under saturated conditions. The slight differences and fluctuations observed in the measured evaporation rates during Stage-1 in our experiments are mostly due to the fluctuation in airspeed (Poós and Varju, 2020). As shown in Fig. 3 (b), in all cases, the slopes of the cumulative mass loss curves were initially high (indicating a high evaporation rate which corresponds to Stage-1 evaporation) and can be well represented by Equation (1). During this period, the drying process is dominated by the capillary-induced liquid flow from the drying front to the evaporation surface maintaining a high evaporation rate despite the receding drying front. It is expected that BMSFs made from FAC with finer particle sizes will exhibit longer Stage-1 evaporation. Stage-1 evaporation, which is supplied by capillary liquid transport, ends when the moisture content decreases to a lower level, then the evaporation is dominated by vapor diffusion (Stage-2).

The evaporation rate  $J_{v,sat}$  under the saturated state (Stage-1) and the surface mass transfer coefficient,  $h_m$ , which can be obtained using data either from the Stage-1 or Stage-2 evaporation, are summarized in Table 1. The values of  $u_v$  and  $u_a$  were calculated using the READY tools developed by NOAA (Rolph et al., 2017) as functions of the air temperature and relative humidity measured during the experiments.

# 2.3.2. Leveraging surface geometry to enhance evaporation

One unique feature of the BMSF is that the material is 'monolithic' as compared to the granular materials used in many other studies (Wanphen and Nagano, 2009; Shokri Kuehni et al., 2016). Therefore, the surface topology of the BMSF panel can be tailored to enlarge the evaporative surface area at the macro scale to increase the evaporation rate. To this end, BMSF panels with protruded surfaces, either in 'pyramid' or 'frustum' shapes, were tested. Fig. 4 shows the Stage-1 evaporation rate from BMSF panels subjected to the same environmental conditions (i.e., the ambient air temperature was maintained at 30 °C and the relative humidity was maintained at 40%). The evaporation rate of saturated BMSF with the 'pyramid' surface and 'frustum' surface are 7% and 14% higher than that of the open water surface, respectively. The increase in evaporation rate is nearly proportional to the surface areas of the panel - i.e., the total surface area of the 'pyramid' and 'frustum' shaped panels are 25% and 32% higher than the flat surface, which corresponds well with the increase in evaporation rate as shown in Fig. 4. This creates opportunities to create building surfaces with very

**Table 1** Experimental surface mass transfer coefficients.

Condition		u <sub>v</sub> [kg/	u <sub>a</sub> [kg/	$h_m$ [m/	$J_{\nu,sat}$ [kg/ $(m^2 \cdot s)$ ]
Air temperature [°C]	Relative humidity [%]	m <sup>3</sup> ]	m <sup>3</sup> ]	s]	
20	40	0.0172	0.0069	0.0103	$1.067 \times 10^{-4}$
30	40	0.027	0.012	0.0102	$1.520 \times 10^{-4}$
40	40	0.0402	0.0202	0.0097	$1.942 \times 10^{-4}$
25	60	0.0222	0.0137	0.0114	$9.730 \times 10^{-5}$
25	80	0.0229	0.0183	0.0112	$5.115 \times 10^{-5}$

high evaporation rates, and thus cooling effects, by engineering surfaces that have enlarged surface area while promoting airflow. The optimized topologies can be easily realized through 3D printing; however, it lies outside the scope of this paper.

#### 2.4. Thermal conductivity

The thermal conductivities of BMSF (dry), BMSF (saturated), and concrete samples were measured using the transient plane source (TPS) method via a *HotDisk TPS2500* thermal constant analyzer, see Fig. 5 (a). For the test, two identical samples were prepared with their surfaces polished and washed. The samples were kept in a convection oven at 110 °C for 12 hours before they were conditioned for TPS testing. During the test, a Kapton that supported a double-spiral nickel metal sensor was placed between two samples, as shown in Fig. 5 (b). The sensor performs as the source of producing heat while measuring the temperature at the same time. In the TPS test, the initial electrical resistance of the TPS element was first balanced in a Wheatstone bridge. Later, the unbalanced voltage drop was captured as a function of time by a highimpedance digital voltmeter. As a result, the thermal conductivity and thermal diffusivity were measured and reported through an iteration. The measured thermal properties of the BMSF and concrete samples are presented in Table 2.

# 2.5. Surface light reflectance

The diffusive solar reflectance of BMSF (under both dry and saturated conditions) and a concrete benchmark was measured using a UV-VIS-NIR spectrophotometer in conjunction with an integrating sphere attachment based on ASTM E903 specifications (Performance et al., 1996). The spectrophotometer (StellarNet Black Comet) can measure the spectral characteristics of the test specimen over the spectral region from approximately 300 nm-1200 nm. The integrating sphere is a wall-mounted type such that the specimen can be placed in direct contact with the rim of an aperture in the sphere wall for reflectance measurements, see Fig. 6. A metal halide light source was used for the measurements, see Fig. 6 (a). The light source used for this measurement provides spectra in the range of 300 nm-750 nm, see Fig. 6 (b). During the experiment, a high-reflectance reference specimen (barium sulfate) was used to measure and record the 100% line; the zero line was recorded in a totally dark environment. The BMSF specimen under both dried and saturated conditions and a concrete benchmark specimen were then measured, and the spectral reflectance,  $\tau(\lambda)$ , at the wavelength  $\lambda$ , was calculated by:

$$\tau(\lambda) = \frac{S_{\lambda} - Z_{\lambda}}{100_{\lambda} - Z_{\lambda}} \tag{2}$$

where  $100_{\lambda}$  is 100% correction obtained with the specimen port replaced by a sample having a coating and a curvature identical to the sphere wall. The zero-line correction is negligible.  $S_{\lambda}$  is recorded specimen reading.  $Z_{\lambda}$  is zero-line reading.

The average absorptance  $\overline{a}$  under incoming radiation  $I(\lambda)$  is obtained by the following equation:

$$\overline{\alpha} = 1 - \frac{\int_{0}^{\infty} \tau(\lambda)I(\lambda)d\lambda}{\int_{0}^{\infty} I(\lambda)d\lambda}$$
(3)

Fig. 6 (b) presents the spectral characteristics of concrete, BMSF (dried), and BMSF (saturated), where the average absorptance over the measured spectrum was calculated as 60.0% for concrete, 56.4% for dried BMSF, and 61.2% for saturated BMSF, see Fig. 6 (b).

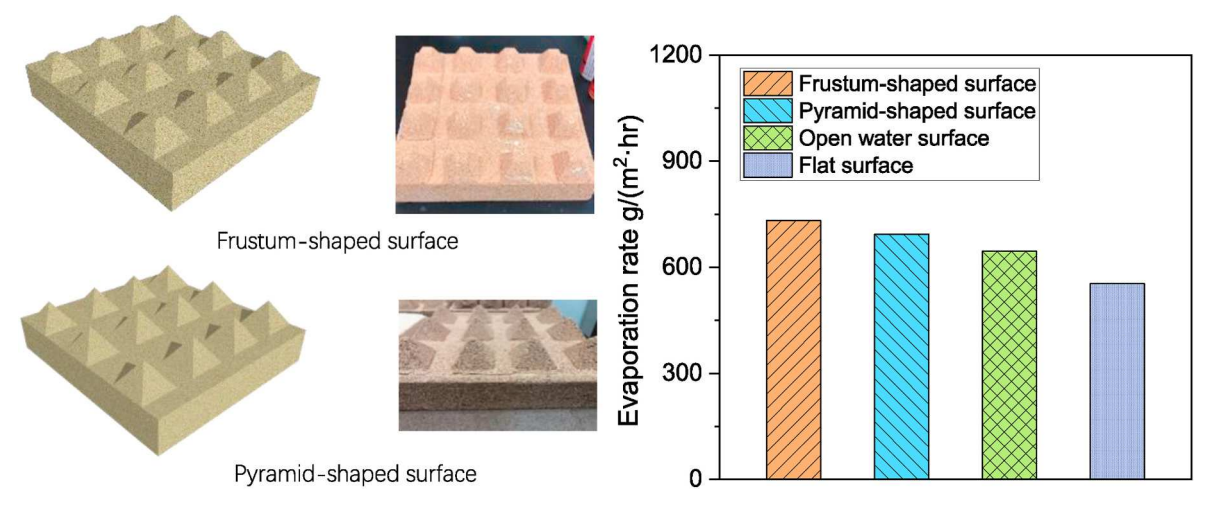


Fig. 4. Evaporation rate of saturated BMSFs with different surface configurations.

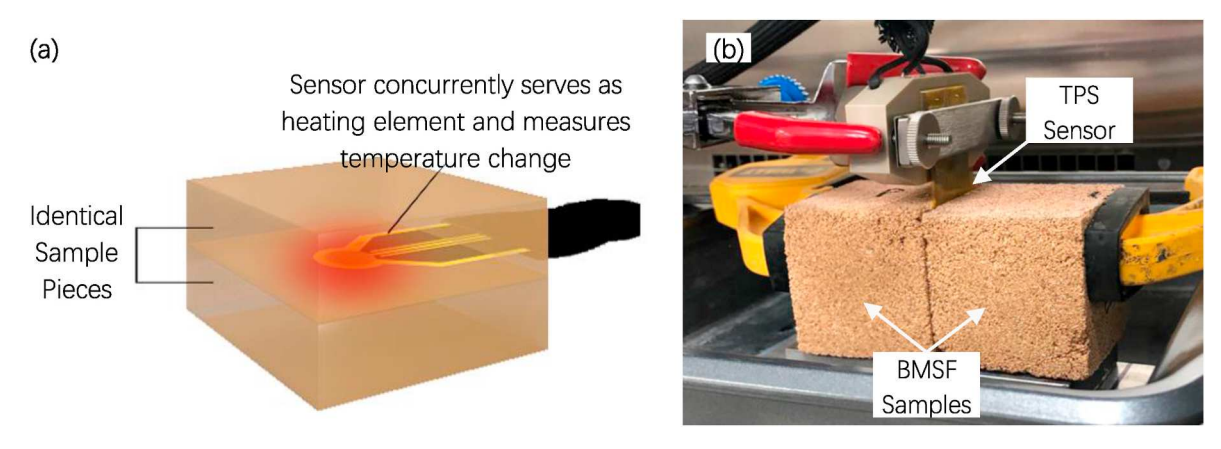


Fig. 5. Transient plane source test to measure the thermal constants of materials: (a) illustrative figure; and (b) experimental setup for the BMSF foam.

Table 2 Material properties of the test panels.

Material	Density [kg/m³]	Thermal conductivity <sup>a</sup> [W/(m·K)]	Specific heat <sup>b</sup> [J/ (kg·K)]	Average solar absoptance <sup>c</sup>
Saturated BMSF panel	$825\pm12$	$0.445\pm0.042$	$969.70 \pm \\12.37$	$0.61\pm0.02$
Dry BMSF panel	$473 \pm 5.7$	$0.1964 \pm 0.0121$	$746.51 \pm \\ 24.30$	$0.54\pm0.01$
Concrete panel	$\begin{array}{c} \textbf{2342} \pm \\ \textbf{54} \end{array}$	$2.483 \pm 0.24$	$753.63 \pm \\15.50$	$0.60\pm0.02$

<sup>&</sup>lt;sup>a</sup> Thermal conductivity was measured using transient plane source (TPS) method according to ISO22007 specifications.

### 3. Surface cooling behavior of BMSF: experiment and simulation

# 3.1. Thermal network model to consider evaporative cooling on building surfaces

A thermal network model based on the finite difference method is developed herein to simulate the thermal behavior of building roofs covered with BMSF panels. The heat transfer equations were established by the heat balance within each finite volume represented by the thermal nodes shown in Fig. 7. The heat balance at the exterior surface node of the BMSF panel considers effects due to convective heat exchange, heat conduction, short-wave radiation,  $Q_{i,sw,b}$ , long-wave radiation,  $Q_{i,lw}$ b and latent heat from evaporation,  $Q_{i,lat,b}$ , which can be expressed as:

$$\begin{split} \int\limits_{V_{i,b}} \rho_b c_{p,b} dV_{i,b} \frac{dT_{i,b}}{dt} &= H_{i,b}^{air-ex} \left( T_{air-ex} - T_{i,b} \right) + H_{i,b}^{i-1} T_{i-1} + H_{i,b}^{i+1} T_{i+1} \\ &- \left( H_{i,b}^{i-1} + H_{i,b}^{i+1} \right) T_{i,b} + Q_{i,sw,b} + Q_{i,lw,b} + Q_{i,lat,b} \end{split} \tag{4-a}$$

$$Q_{i,sw,b} = \overline{\alpha}_{i,b} I_s^{\downarrow} A_{i,b} \tag{4-b}$$

$$\begin{aligned} Q_{i,lw,b} &= \left[F_{i}^{sky}\left(T_{sky,abs}^{4} - T_{i,abs,b}^{4}\right) + F_{i}^{grd}\left(T_{grd,abs}^{4} - T_{i,abs,b}^{4}\right) + F_{i}^{airex}\left(T_{airex,abs}^{4} - T_{i,abs,b}^{4}\right)\right] \\ &\cdot \sigma \varepsilon_{i,b} A_{i,b} + \sum_{k} \sigma \varepsilon_{i,b} F_{i}^{k}\left(T_{k,abs}^{4} - T_{i,abs,b}^{4}\right) A_{k} \end{aligned}$$

 $Q_{i,lat,b} = E_{LT} h_{i,m,b}^{air\_ex} (u_{i,b} - u_{air\_ex}) A_{i,b}$ (4-d)

(4-c)

(4-e)

$$h_{i,m,b}^{air\_ex} = \frac{h_{i,c,b}^{air\_ex}}{\rho_{air\_ex}c_{p,air\_ex}} Le^{-\frac{2}{3}}$$
 (4-e)

$$h_{icb}^{air-ex} = 6.47 + 6.806v_{ex}$$
 (4-f)

where  $H_{i,b}^{j}$  is heat transfer coefficient between air node j and BMSF surface node *i*; *V* is volume;  $\overline{a}_{i,b}$  is solar absorptance;  $F_i^k$  is view factor for

b Specific heat was estimated using TPS method based on thermal diffusivity.

<sup>&</sup>lt;sup>c</sup> Solar absorptance was measured using spectrophotometer with integrating sphere.

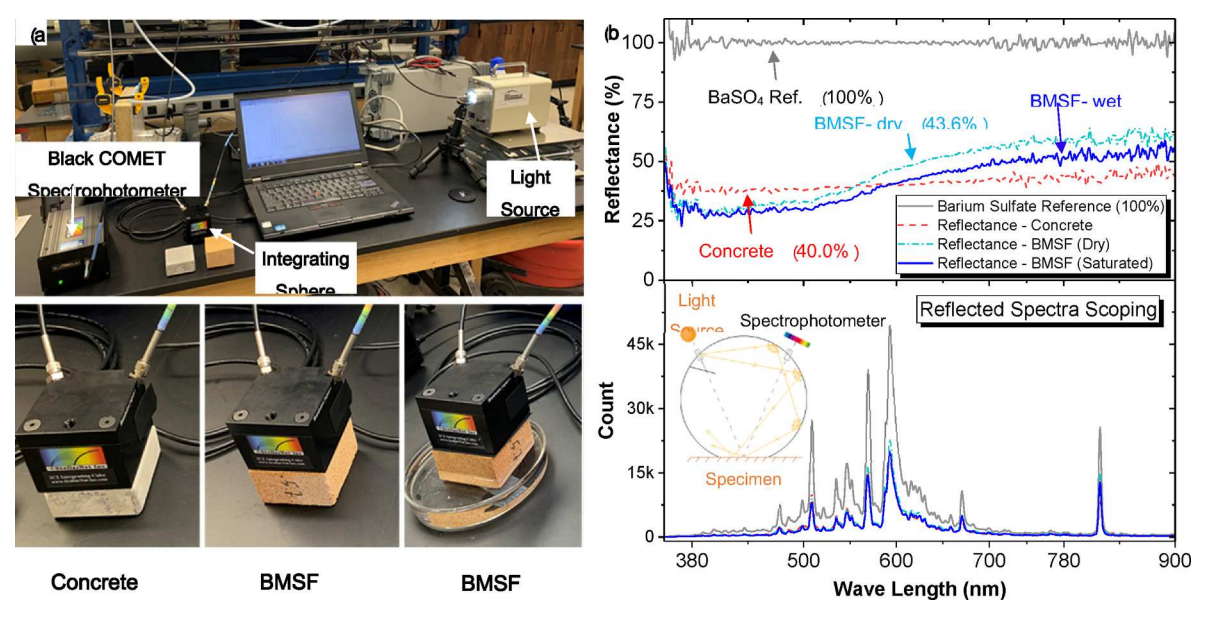


Fig. 6. (a) Experimental setup to determine the surface light reflectance of concrete and BMSF surfaces using UV-VIS-NIR spectrophotometer and integrating sphere (b) Measured spectral reflectance of the specimens.

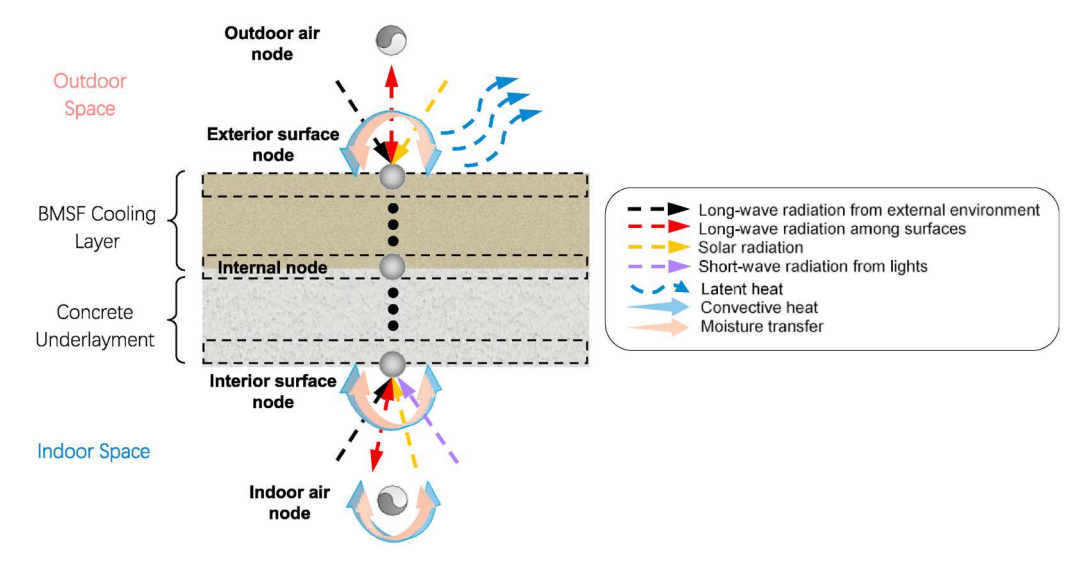


Fig. 7. Thermal network model of concrete roof covered with BMSF panel.

node i with exterior emitting surface k – i.e., wall or window surfaces;  $E_{LT}$  is latent heat per unit mass of water evaporation;  $h_{i,m,b}^{air\_ex}$  is surface mass transfer coefficient between outdoor air and BMSF surface node i;  $h_{i,c,h}^{air\_ex}$  is surface heat transfer coefficient between outdoor air and BMSF surface node i; The classic empirical formula adopted in ASHRAE/DOE-2 model (Palyvos, 2008; MehrangizJHK, 1994) in Equation (4-f) is used for surface heat transfer coefficient calculation; Le is the Lewis number – a dimensionless number defined as the ratio of thermal diffusivity to mass diffusivity (Kloppers and Kröger, 2005);  $v_{ex}$  is air velocity. Other notations in Equation (4) can be found in the nomenclature. In this research, a continuous water supply (dripping pipe) was provided to maintain the BMSF panel under saturated conditions. A water barrier was placed between the BMSF panel and the concrete roof to prevent moisture transfer between the BMSF layer and the adjacent concrete layer, thus only heat conduction takes place at the interface between BMSF and the concrete roof substrate.

For internal nodes (non-surface nodes) within the envelope layers, only heat conduction takes place:

$$\int_{V_{i,w}} \rho_{i,w} c_{p,w} dV_{i,w} \frac{dT_{i,w}}{dt} = H_{i,w}^{i-1} T_{i-1} + H_{i,w}^{i+1} T_{i+1} - \left(H_{i,w}^{i-1} + H_{i,w}^{i+1}\right) T_{i,w}$$
(5)

The heat balance at the interior surface node (indoor surface) considers short-wave radiation from lighting  $Q_{i,lw}^{light}$ , long-wave radiation from occupant activities  $Q_{i,lw}^{people}$ , lighting  $Q_{i,lw}^{light}$  and equipment  $Q_{i,lw}^{equip}$  applied on interior surfaces.

$$\int_{V_{i,w}} \rho_{i,w} c_{p,w} dV_{i,w} \frac{dT_{i,w}}{dt} = H_{i,w}^{j} \left( T_{j} - T_{i,w} \right) + H_{i,w}^{i-1} T_{i-1} + H_{i,w}^{i+1} T_{i+1} \\
- \left( H_{i,w}^{i-1} + H_{i,w}^{i+1} \right) T_{i,w} + Q_{i,tw,w} + Q_{i,tw,w}$$
(6-a)

$$Q_{i,sw,w} = \overline{\alpha}_{i,w} I_s^{\downarrow} A_{i,w} + Q_{i,sw}^{light}$$
(6-b)

$$Q_{i,lw,w} = \sum_{k} \sigma \varepsilon_{i,w} F_i^k \left( T_{k,abs}^4 - T_{i,abs,w}^4 \right) A_k + Q_{i,lw}^{people} + Q_{i,lw}^{light} + Q_{i,lw}^{equip}$$
(6-c)

The heat transfer process for indoor air includes convective heat exchange with interior wall and window surfaces, air conditioning, infiltration and absorption of heat from internal gains  $Q_{j,int}$  generated by occupant activity  $Q_{j,conv}^{people}$ , lighting  $Q_{j,conv}^{light}$ , and equipment  $Q_{j,conv}^{equip}$ . The heat balance of the indoor air node j can be written as:

$$\begin{split} & \rho_{j}c_{p,j}V_{j}\frac{dT_{j}}{dt} = \sum_{k}H_{j}^{k}\left(T_{k}-T_{j}\right) + c_{p,j}\dot{m}_{j}^{sys}\left(T_{sup,j}-T_{j}\right) + c_{p,j}\dot{m}_{j}^{inf}\left(T_{air\_ex}-T_{j}\right) \\ & + Q_{i.int} \end{split}$$

(7-a)

$$Q_{j,int} = Q_{j,conv}^{people} + Q_{j,conv}^{light} + Q_{j,conv}^{equip}$$
(7-b)

where  $m_j^{\text{sys}}$  and  $m_j^{\text{inf}}$  are mass flow rate into the indoor zone for air node j from the air conditioner and outdoor air, respectively;  $T_{sup,j}$  is the supply air temperature of the air conditioner for indoor air node j.

The moisture balance for indoor air node *i* is:

$$\dot{W}_j = w_i^{int} + w_j^{sys} + w_j^{inf} \tag{8}$$

where  $W_j$  is water mass of indoor air node j;  $w_j^{int}$ ,  $w_j^{sys}$  and  $w_j^{inf}$  are moisture transfer rate for indoor air node j from internal latent heat gains, air conditioning systems and infiltration, respectively. Detailed equations for the nodal network formulation can be found in the previous work of the authors (He et al., 2020).

# 3.2. Experimental setup and instrumentation

In order to investigate the thermal performance of the BMSF panel, experiments were carried out to study its ability to modulate the building roof surface temperature and reduce heat fluxes penetrating into the indoor space through comparisons among the bare concrete panel, the concrete panels covered with dry and wet BMSF panels. The

experimental setup is illustrated in Fig. 8, where the test specimen and test apparatus were placed in an environmental chamber (ESPEC Inc.) to allow adjustment of ambient temperature and relative humidity (RH) throughout the course of the experiment. For the control test, a 200 mm by 200 mm and 38 mm thick concrete specimen was instrumented with thermocouples attached to the top and bottom surfaces and heat flux sensors attached to the bottom surface. In order to create the temperature differential needed for the experiment, a water-cooled cold plate was placed on the bottom surface of the concrete specimen. The test specimens, together with the cold plate, were encased in a tightly insulated box to create near 1-D heat flow, see Fig. 8 (a) and (b). The temperatures at both the top and bottom surfaces of the concrete specimen were measured throughout the experiment. The bottom surface of the concrete specimen was in contact with the cold plate, the temperature at point  $T_{c,b}$  (see Fig. 8 (a)) varied based on the heat flux flowing through the test specimen. For the BMSF-enhanced roof specimen, the BMSF layer (38 mm thickness) was overlaid on the top of a 38 mm thick concrete panel. The specimen was wrapped in aluminum foil to prevent water loss on all boundaries except the top surface, which was exposed to air for evaporation. The BMSF panel was saturated with water and an adjustable water dripping line was installed to supply water during the evaporation process. To measure the water consumption, the water supply tanks were mounted on digital balances (with the accuracy of 0.1 g) and connected to a computer to record the mass change every 2 seconds during the experiments. A thermocouple probe was used to measure the inlet water temperature during the experiment. The specimens were instrumented with multiple thermocouples (Omega Engi*neering*) placed at both the top and bottom surfaces of the concrete panel as well as the top surface of the BMSF panel to measure temperature changes. Since a metal halide light was used as the heat source, temperature variations were expected across sample surfaces. Therefore, surface temperatures were averaged from the thermocouple reading at different locations (Liao et al., 2020, 2021).

In addition, heat flux sensors (FluxTeq Inc.) were attached to both the

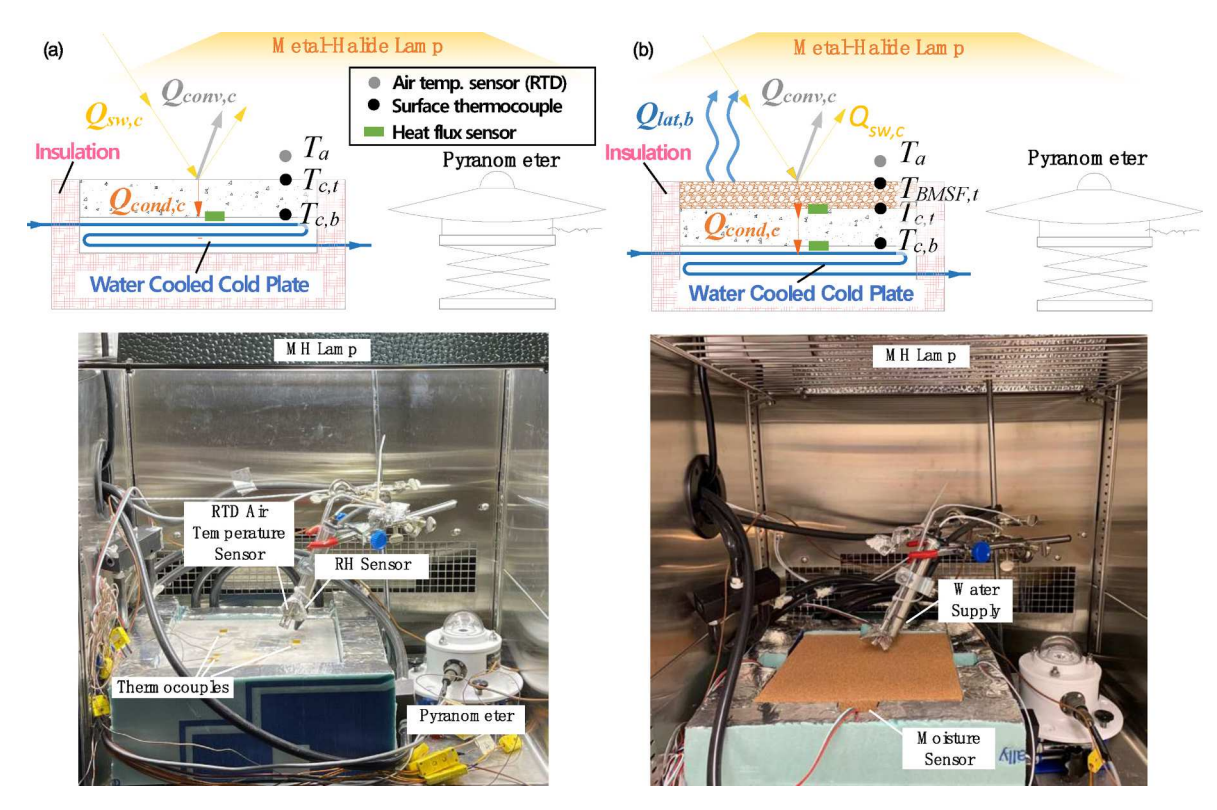


Fig. 8. Experimental setup and instrumentation for testing the cooling behavior of the BMSF roof overlay: (a) setup to test the concrete benchmark (a metal halide lamp was used to simulate the solar exposure); (b) test of BMSF overlay where a 38 mm thick BMSF panel overlaid on top of the concrete panel (water supply was turned on and off to test the BMSF under both dried and wetted condition).

top and bottom surfaces of the concrete panel with BMSF to measure the heat fluxes going through these planes, see Fig. 8. An RTD air temperature sensor and a solid-state relative humidity (RH) sensor were placed approximately 25 mm above the top surface of the test panels to measure the air temperature and relative humidity change near the panel surface. The temperature sensors were shielded using aluminum foil domes to avoid direct heating from irradiation. The data were recorded using a National Instrument PXI-express data acquisition system at every 2second interval throughout the course of the experiment. To simulate the solar radiation, a 400 Watts metal halide (MH) bulb was installed in the environmental chamber, which was fixed on customized stands facing the test panels. A pyranometer (Eppley Laboratory, Inc.) was used to measure the shortwave radiation from the MH bulb. The height of the specimens was adjusted such that both the BMSF and the concrete roof baseline were exposed to a similar level of irradiation. During the tests, the incident irradiance from MH light was measured at around 350 W/ m<sup>2</sup> at the panel surface level, the air temperature was controlled at around 35 °C, and the RH was controlled at around 40%.

# 3.3. Results and discussion

Figs. 9–11 present the experimental results obtained from the concrete benchmark specimen and the BMSF overlaid concrete specimens under both dried and saturated conditions, respectively. The results of the experiment described in Section 3.2 were also compared with simulated results based on the thermal network model developed in Section 3.1 to calibrate the parameters for case studies in Section 4. The measured data showed that the air temperature near the panel surface was controlled at approximately 35 °C–36 °C across all three experiments. In comparison with the concrete benchmark panel, the temperature measured at the top surface of the concrete ( $T_{c,t}$ ) is significantly lower for the concrete roof panel covered with BMSF due to the shading and cooling effects from the BMSF layer. The temperatures measured at

the bottom surface of the concrete panel  $(T_{c,h})$ , where it is in contact with a water-cooling cold plate (Fig. 8), are different for the benchmark concrete panel (i.e., 36 °C) and the ones with BMSF overlay (i.e., 25  $^{\circ}$ C-27  $^{\circ}$ C). This is mainly due to the low thermal resistance of the concrete panel – i.e., the cooling from the cold plate cannot keep up with the heat flow transferred from the hot radiated surface, resulting in a much higher temperature at the concrete panel's bottom surface. When the BSMF panel is dry, the surface temperature of BMSF  $(T_{BMSF})$  under simulated solar irradiation is higher ( $\sim$ 47.5  $^{\circ}$ C) than that of the concrete surface due to the additional insulation from the BMSF layer (i.e., BMSF has low thermal conductivity when it is dry) - i.e., the radiant heat is being cooled by the cold plate at a much higher rate for the benchmark concrete panel. This is also substantiated by the measured heat flux values (Figs. 9-11), where the heat flux going through the bottom surface of the concrete panel was measured at ~245W/m<sup>2</sup> for plain concrete, around 100W/m<sup>2</sup> for concrete + dry BMSF, and around 75W/m<sup>2</sup> for concrete + wet BMSF. When the BMSF layer is wetted (Fig. 11), the surface temperature of the BMSF layer was drastically reduced to around 35 °C, which is about the same as the ambient air temperature. As compared to the concrete roof panel with dry BMSF, the temperature at the top surface of the concrete panel was reduced by approximately 2.5 °C. The heat flux measured through the concrete panel also indicates that evaporative cooling reduces the amount of heat flow going through the interior surface of the roof assembly, which will in turn reduce the cooling load of the HVAC system. Fig. 11 (a) shows the inlet water temperature and degree of saturation (%) of the BMSF panel measured by four soil moisture sensors throughout the experiment. The inlet water temperature was kept constant near the room temperature of the lab, which is lower than the radiated roof surface. Therefore, the cooling effect shown in Fig. 11 is partly attributed to the lower water temperature similar to the spray cooling system discussed by Nayak et al. (ketanHagishima and Tanimoto, 2020). It is noted that since BMSF has very high porosity in the micrometer size range, water transport within

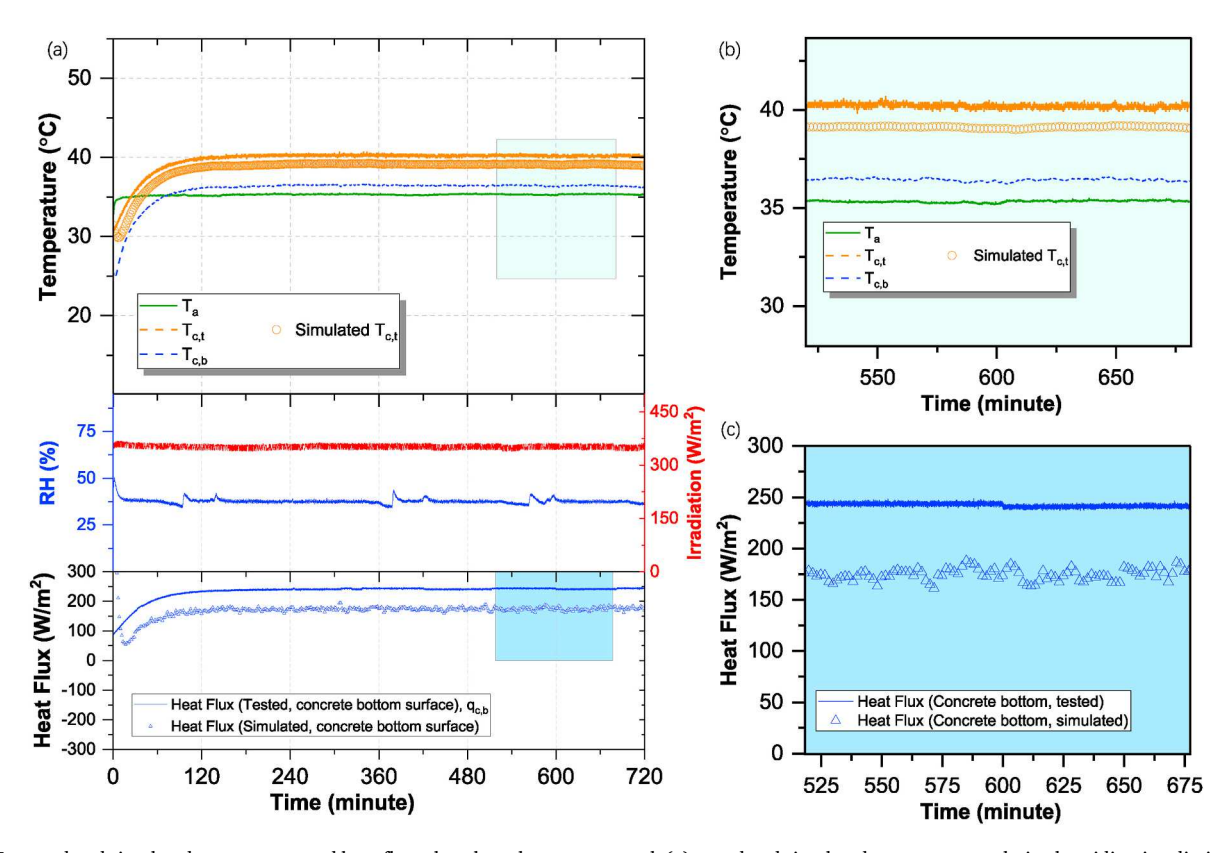


Fig. 9. Measured and simulated temperature and heat flux – benchmark concrete panel: (a) tested and simulated temperature, relative humidity, irradiation and heat flux data; (b) zoom-up view of temperature profile near steady-state condition; and (c) zoom-up view of heat flux profile near steady-state condition.

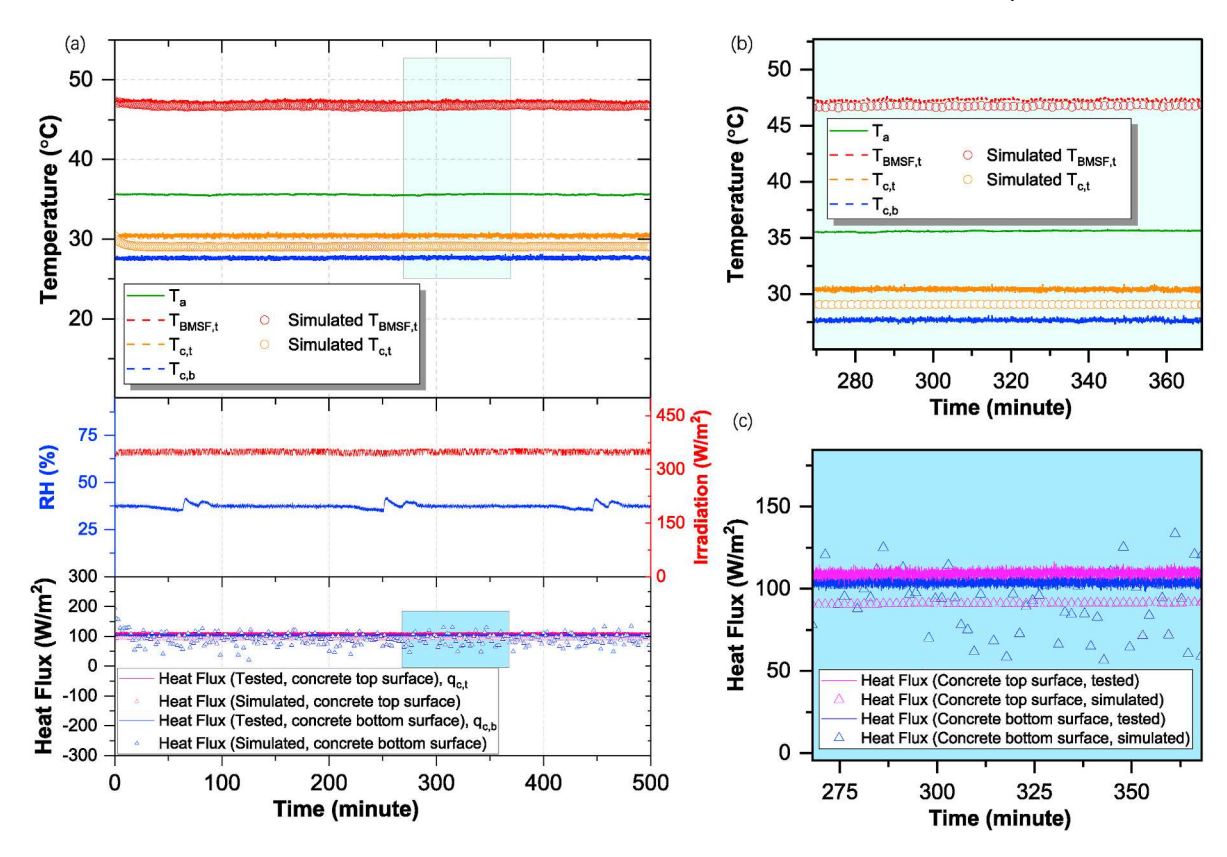


Fig. 10. Measured and simulated temperature and heat flux – concrete + dry BMSF foam: (a) tested and simulated temperature, relative humidity, irradiation and heat flux data; (b) zoom-up view of temperature profile near steady-state condition; and (c) zoom-up view of heat flux profile near steady-state condition.

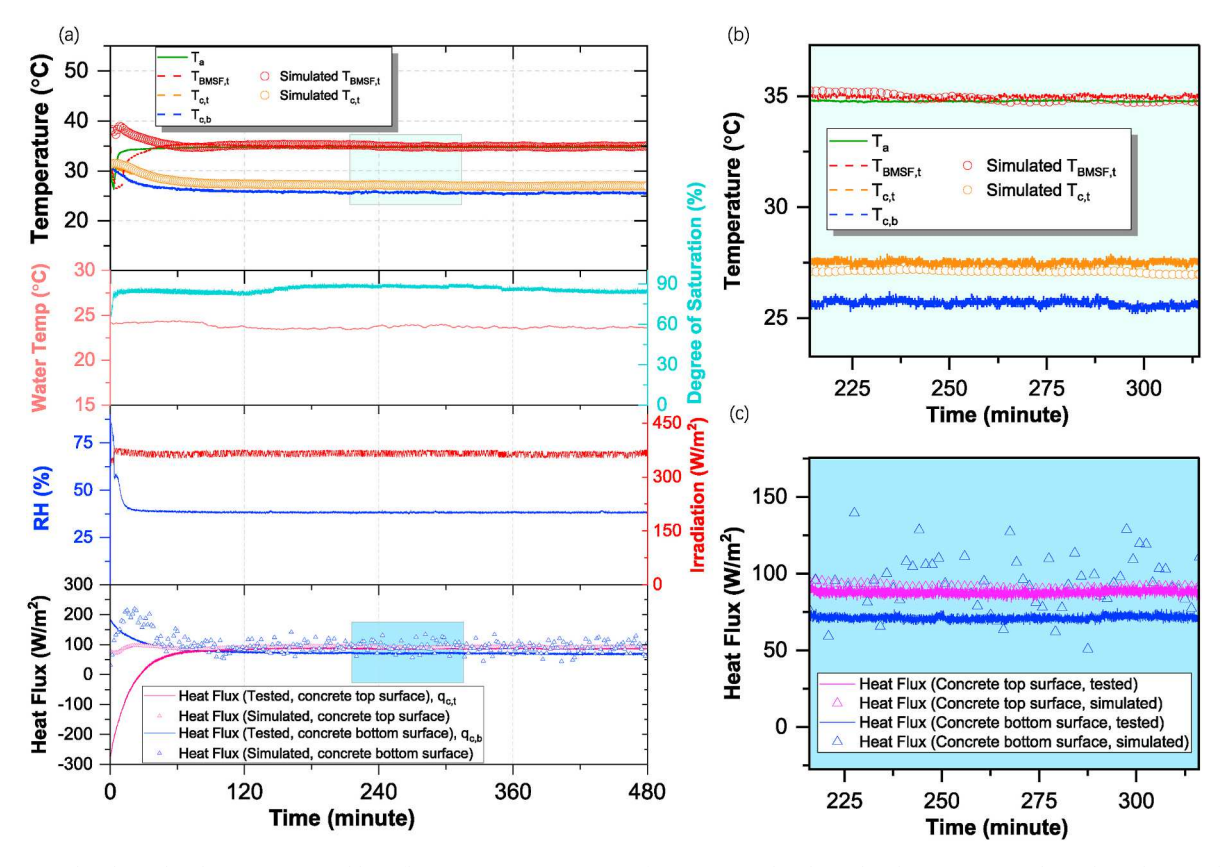


Fig. 11. Measured and simulated temperature and heat flux – concrete + wet BMSF foam: (a) tested and simulated temperature, relative humidity, irradiation and heat flux data; (b) zoom-up view of temperature profile near steady-state condition; and (c) zoom-up view of heat flux profile near steady-state condition.

the material is mainly driven by the capillary effect (Liang et al., 2020), leading to its excellent ability to retain water for prolonged effects of cooling – the study conducted by Kuehni et al. (Shokri Kuehni et al., 2016) indicated that the smaller the pore size of the drying medium, the longer the cooling period will last for a certain amount of available water.

To simulate the experimental condition and calibrate the thermal network model for whole-building energy simulation, only heat transfer through the panels was analyzed in the simulation - i.e., the heat balance of indoor air in Equation (7) was not modeled since the bottom surface of the concrete is in direct contact with a cold plate. Since all surfaces of the specimens were insulated except for the top and bottom surfaces, 1-D heat transfer was considered. The thermal properties of the concrete were assumed to be constants as a water barrier was placed between the concrete panel and the BMSF panel. Thermal contact between the panels was assumed to be ideal so that interface resistance was negligible. Moreover, the long-wave radiation was considered negligible under experimental conditions. Therefore, for the surface node at the BMSF exterior surface, the term  $Q_{i,lw,b}$  is negligible in Equation (6-a); for the node at the top surface of the concrete layer,  $Q_{i,lw,b}$  and  $Q_{i,lat,b}$  are also neglected in the simulation. The surface heat transfer coefficient  $h_{i,c,b}^{air\_ex}$  is calculated by Equation (4-f). Since the bottom surface of the concrete panel is in contact with a cold plate, the temperature measured at this surface  $T_{c,b}$  was used as a boundary condition. The boundary conditions for the top exposed surface are determined by the air temperature  $T_a$  and relative humidity RH measured near the top surface, irradiation intensity measured by the pyranometer, estimated wind speed across the surface (0.5 m/s), and the estimated evaporation rate based on the equations listed in Section 2.3.

Fig. 9 shows simulated top concrete surface temperature  $T_{c,b}$  and the heat flux at the bottom surface of the benchmark concrete specimen in comparison with the experimentally measured values. Figs. 10 and 11 present the simulated temperatures at the top surface of the BMSF foam  $T_{BMSF,t}$ , the top surface of the concrete layer  $T_{c,b}$  and the heat fluxes at both the top and bottom surface of the concrete panel  $-q_{c,t}$  and  $q_{c,b}$ , for the concrete roof panel with dry BMSF overlay and water-saturated BMSF overlay, respectively. Both the simulated temperature profiles and the simulated heat fluxes show good agreement with the experimental data. This indicates that the empirical formula proposed by reference (Palyvos, 2008; MehrangizJHK, 1994) is applicable for heat transfer coefficient and mass transfer coefficient calculation.

# 4. Case study

# 4.1. Simulation details

To investigate the thermal behavior and quantify energy saving potential of building roofs equipped with the BMSF evaporative cooling panel, case studies were conducted using the case of a single-story commercial building through comparisons between the baseline roof and BMSF roofs through simulation analyses with the thermal network model illustrated in Section 3.1 (MATLAB), see Fig. 12. For the case studies, two scenarios of roof insulations were designed to study the effects of BMSF under different insulation levels, where the case  $R_{\rm H}$  has

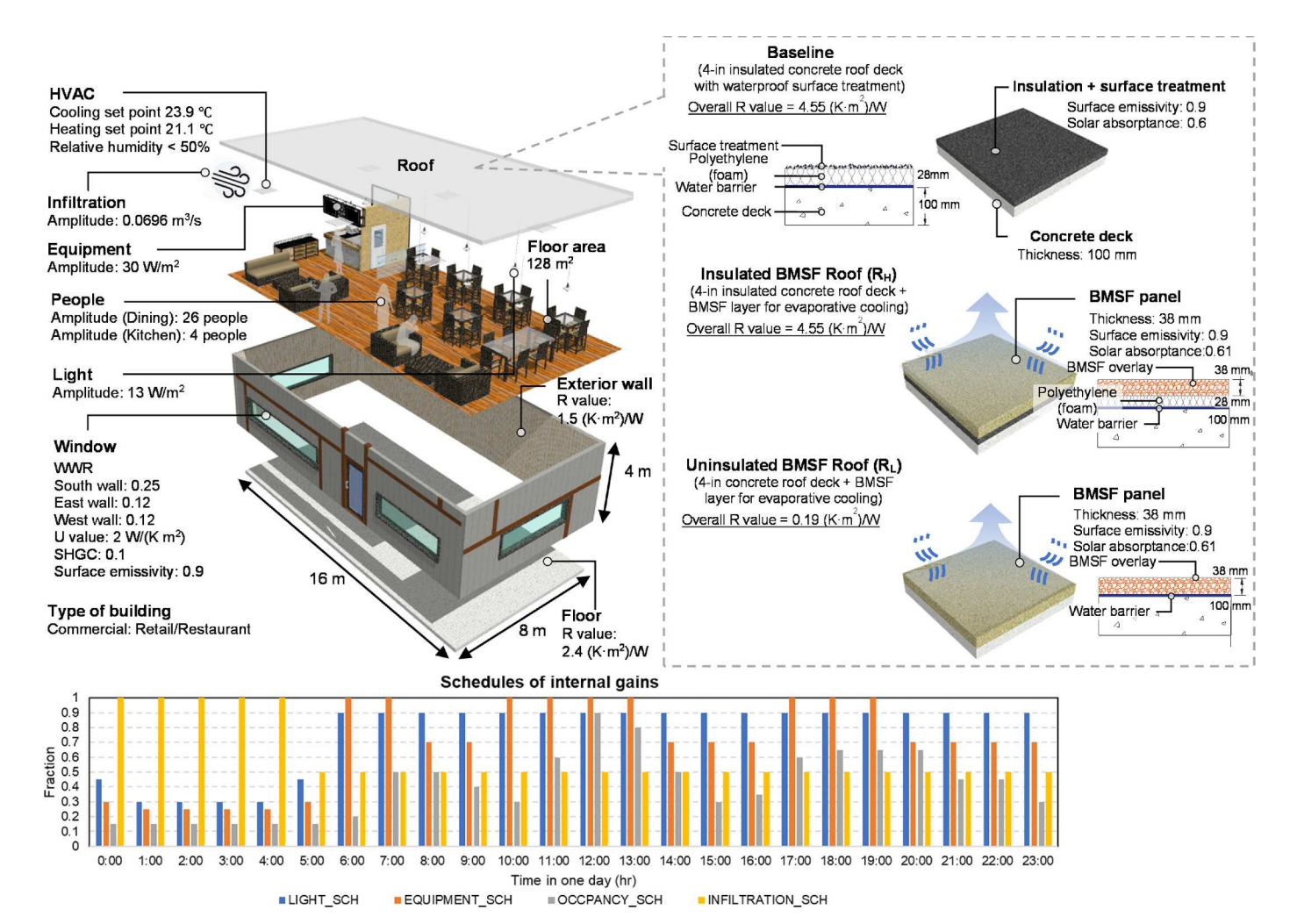


Fig. 12. Simulation case details for buildings with BMSF roofs and baseline concrete roof.

standard RSI-value ( $R=4.55~(\text{K}\cdot\text{m}^2)/\text{W}$ ) according to the specification of ASHRAE 90.1 (Edition et al., 2013); another case  $R_L$  was designed as a BMSF and concrete only roof with no additional insulation ( $R=0.19~(\text{K}\cdot\text{m}^2)/\text{W}$ ) given the cooling effect from evaporation as the alternative for high insulation in summer, see Fig. 12. The purpose of case  $R_L$  was to demonstrate that in certain scenarios (e.g., buildings with high internal load), low thermal resistance building envelopes can augment the cooling effect of evaporative cooling surfaces.

In the case study, material properties (density, thermal conductivity, specific heat, solar absorptance) parameters used for the calculation of surface mass transfer coefficient and surface heat transfer coefficient for BMSF panel and concrete are assumed the same as the measured values presented in Tables 1 and 2 and formulas presented in Section 3. The building dimensions are 16 m (L)  $\times$  8m (W)  $\times$  4 m (H) and the mean window-to-wall ratio is 12.3% for the exterior walls. Other simulation parameters including occupant activities, lighting, equipment, and infiltration are enlisted in Fig. 12. Typical meteorological year 3 (TMY3) weather data of Los Angles, California was used for the simulation.

# 4.2. Thermal behavior of evaporative cooling roof with BMSF panel

Building energy simulation and thermal comfort analyses were conducted on the cafeteria during a representative summer. Fig. 13 (a) shows the simulated roof surface temperatures for both the baseline (without BMSF) and the BMSF roof with standard insulation ( $R_{\rm H}=4.55~({\rm K\cdot m^2})/{\rm W}$ ) and an uninsulated case ( $R_{\rm L}=0.19~({\rm K\cdot m^2})/{\rm W}$ ). The exterior roof surface temperature was greatly reduced by the BMSF panel in comparison with that of the baseline due to shading and the evaporative cooling effects from the BMSF panel. For the case study scenarios, the surface temperature of the baseline concrete roof with standard R-value ( $R_{\rm H}$ ) reaches around 45 °C in summer, whereas it remained around 30 °C for the BMSF evaporative cooling roof. This is consistent with the experimental observations in Section 3.3. It is noted that due to the high

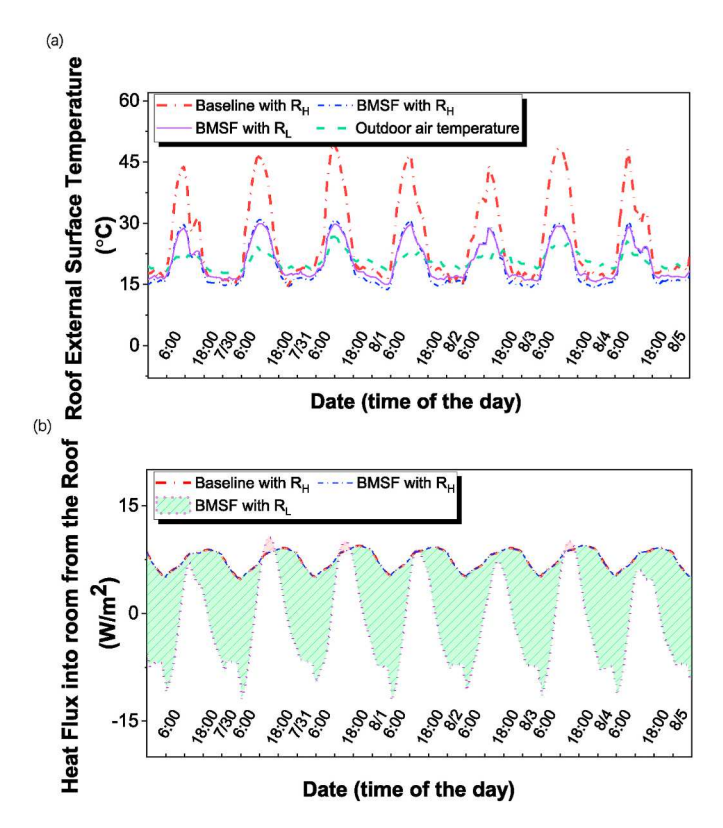
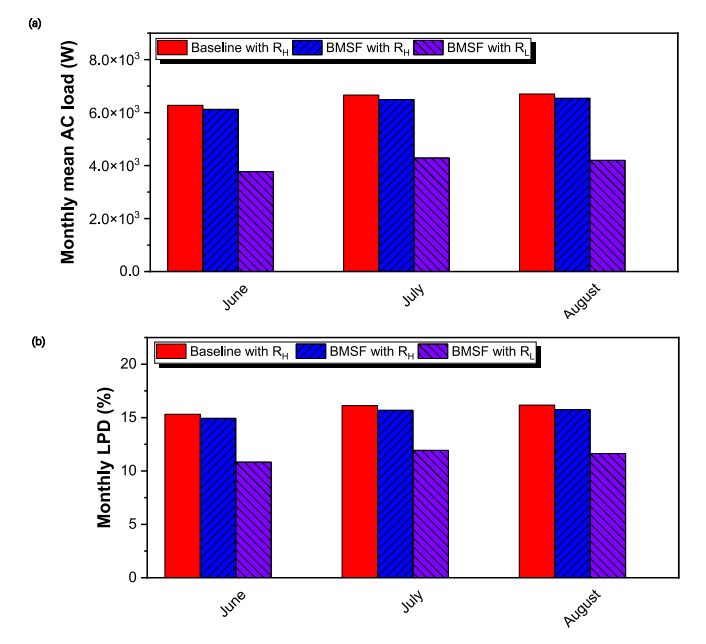


Fig. 13. Comparison between baseline roof and the BMSF roof with standard insulation ( $R_{\rm H}$ ) and low insulation ( $R_{\rm L}$ ): (a) roof surface temperature; and (b) heat flux.

internal load level of a cafeteria during the daytime and the relatively mild outdoor temperature, high insulation building envelopes may act adversely and lead to high energy consumption for the HVAC system – i. e., most of the unwanted heat from internal loads (i.e., occupants, equipment, and lighting) must be cooled by HVAC. In this case, evaporative cooling can effectively reduce the cooling load by allowing the unwanted heat to flow from the indoor space to the outdoor environment. Therefore, for this case study, an uninsulated case  $(R_{\rm L})$  is examined where the uninsulated building roof can maximize the cooling effect from the evaporative cooling surface. Fig. 13 (b) compares the heat fluxes flowing from the roof and into the indoor space during representative summer days. The peak heat flux reduction through the roofs by the BMSF with standard R-value (RH) is around 8.7% during summer days while the heat flux of the uninsulated case  $(R_{\rm L})$  fluctuates much more drastically throughout the diurnal cycles due to the low thermal resistance. For mild climate regions like Los Angeles (climate zone 3B), the outward flowing heat flux during the nights allows the removal of unwanted heat from the high internal loads to help reduce the cooling load of the HVAC system. Comparing the cases between the BMSF roof with  $(R_{\rm H})$  and without  $(R_{\rm I})$  insulation, the uninsulated BMSF roof  $(R_{\rm I})$  provides additional cooling to cope with the building's high internal load while maintaining a relatively low positive heat flux during daytime (the shaded area between the blue dash-dotted line and violet dashed line in Fig. 13 (b)).

# 4.3. Energy saving potential and thermal comfort performance

Fig. 14 presents the comparison of energy performance of the studied cases with different roof designs -i.e., insulated concrete baseline ( $R_{\rm H}$ ), insulated concrete + BMSF ( $R_{\rm L}$ ), and uninsulated concrete + BMSF ( $R_{\rm L}$ ). Fig. 14 (a) presents monthly mean AC loads for buildings with both the baseline roof and BMSF roofs with different roof designs analyzed herein. The simulation results show that AC load reduction by the BMSF roof with the lower roof insulation level ( $R_{\rm L}$ , 37.6%) is significantly higher than the ones with the high insulation level ( $R_{\rm H}$ , 2.5%) in summer. For buildings in the mild climate and with high internal loads, more energy savings can stem from reducing the roof insulation to augment the cooling effects of the evaporative BMSF roof, which consequently leads to lower interior surface temperatures. As a result, the AC load can



**Fig. 14.** Energy performance of the building installed with baseline roof and BMSF roofs with different insulation levels: (a) monthly mean AC load and (b) monthly LPD.

be effectively shed by evaporative cooling from the BMSF roof during the summer days. High roof insulation in this case hinders the beneficial heat flow into the indoor space from the cooling surfaces. As shown in Fig. 14 (a), the AC load reduction for the  $R_{\rm H}$  case is very marginal. Therefore, in cases when internal gains are substantial, lower roof insulation ( $R_{\rm L}$ ) is beneficial to AC load reduction.

Despite its energy-saving potential, it is well known that the evaporative cooling system needs water for cooling, which may be partially compensated by rainwater precipitated on the roof surface (Spanaki et al., 2011). The water demands of the BMSF with  $R_{\rm H}$  and  $R_{\rm L}$  are 475.7 kg/m² and 501.1 kg/m², respectively. The rainwater available for utilization is 362.0 kg/m² according to historical weather data from NOAA's National Weather Service for the Los Angeles, CA area, such that only a fraction of the water demand needs to be compensated by freshwater support (or reuse of greywater generated from buildings). In addition, with well-designed control and optimization (e.g., water supply can be shut off when cooling demand is low), the water demand may be further reduced – the controller design for the water supply system falls outside the scope of this paper.

The Predicted Mean Vote (PMV) and Predicted Percentage of Dissatisfied (PPD) based on Frager's model (ISO., 2005) are used to evaluate the thermal comfort-time performance of the building. The Long-term Percentage of Dissatisfied (LPD) is used to assess occupants' long-term thermal comfort (Carlucci, 2013). The analysis results show that the BMSF roof reduces the predicted percentage of discomfort in summer. Fig. 14 (b) presents the corresponding monthly long-term percentage of dissatisfied (LPD). LPD of buildings installed with the baseline roof with  $R_{\rm H}$  and BMSF panels with  $R_{\rm H}$  and  $R_{\rm L}$  are 15.9%, 15.5%, and 11.5%, respectively. Similar to the trend of AC load reduction, the thermal comfort improvement by BMSF roof with  $R_{\rm L}$  shows higher potential during summer.

# 5. Conclusions and outlook

In this research, a low-cost, biomimetic inorganic synthetic foam material, namely BMSF, was developed and demonstrated for building surface cooling. The BMSF material is made from an abundant industrial byproduct – i.e., fly ash cenospheres, through a minimal contact method developed by the authors. The material is low-cost and can be mass-produced for large-scale building applications. Microstructural analysis (i.e., X-ray microtopography and scanning electron microscopy) revealed that the microstructure of the BMSF resembles that of the keratinous skin of elephants and certain desert lizards, where the hydrophilic surface and hollow cavity structure of BSMF enable water to be transported and stored effectively within the material through capillary actions.

The thermophysical properties of BMSF were characterized and a series of controlled drying/evaporation experiments were conducted on BMSF panels under combinations of various temperature and relative humidity to quantify the drying behavior and evaporation rate of the material. In addition, experimental studies were also carried out to test the cooling effectiveness of BMSF for building roof cooling applications with a scaled-down concrete roof panel tested in conjunction with the one equipped with BMSF cooling panel. The results demonstrated the promising cooling performance of BMSF – i.e., the surface temperature was reduced by 12.5 °C in comparison with the baseline concrete roof, and heat flux flowing through the concrete panel with BMSF panel was reduced by nearly 65% in comparison with the concrete baseline panel.

Lastly, a case study was conducted on a single-story cafeteria in Los Angeles, California (climate zone 3B) to quantify the energy-saving potential and thermal comfort improvement brought by the BMSF cooling layer. The simulation results show that the BMSF roof with standard insulation (R =  $4.55(\text{K}\cdot\text{m}^2)/\text{W}$ ) provides limited energy saving potential (2.5% AC load reduction compared with baseline with standard insulation level in summer) as the high thermal resistance of roof insulation cut off heat flow from the evaporative surface and therefore

limits the benefit of evaporative cooling. The building roofs with low thermal resistance or the uninsulated ones equipped with BMSF may provide substantial energy savings (37.6% AC load reduction compared with baseline with standard insulation level in summer) and thermal comfort improvement (27.7% LPD reduction compared with baseline with standard insulation level) for buildings in the mild climate and with high internal loads. It is worth noting that evaporative cooling, in general, consumes a large amount of water, which may be compensated by rainwater collection or the reuse of greywater in buildings. The water management aspects and durability of the BMSF material are not included in the discussion of this paper, which are suggested for future studies.

# CRediT authorship contribution statement

Yawen He: Methodology, Model code development, Numerical simulation, Writing - Original draft preparation; Adam Brooks: Experimental study, setup, data processing; Yucen Li: Experimental testing; Hongyu Zhou: Project Administration, Conceptualization, Funding Acquisition, Writing – Reviewing and Editing.

# Declaration of competing interest

The authors declare that they have no known competing financial interests or personal relationships that could have appeared to influence the work reported in this paper.

### Data availability

Data will be made available on request.

# Acknowledgements

This research was made possible by U.S. National Science Foundation (NSF CMMI-1954517), U.S. Department of Energy (DE-EE-0008677), and the startup fund provided by The University of Tennessee, Knoxville. The content of this paper does not reflect the view of the funding agencies.

# References

- Adán, A., Prieto, S.A., Quintana, B., Prado, T., 2019. An autonomous thermal scanning system with which to obtain 3D thermal models of buildings. Adv. Informatics Comput. Civ. Constr. Eng. 489–496. https://doi.org/10.1007/978-3-030-00220-6. Springer International Publishing.
- Al-Sanea, S.A., Zedan, M.F., Al-Hussain, S.N., 2012. Effect of thermal mass on performance of insulated building walls and the concept of energy savings potential. Appl. Energy 89, 430–442. https://doi.org/10.1016/j.apenergy.2011.08.009.
- Athienitis, A., Brien, W.O., 2015. Modeling, Design, and Optimization of Net-Zero Energy Buildings.
- Berardi, U., Garai, M., Morselli, T., 2020. Preparation and assessment of the potential energy savings of thermochromic and cool coatings considering inter-building effects. Sol. Energy 209, 493–504. https://doi.org/10.1016/j.solener.2020.09.015.
- Brick Industry Association, 2006. Technical notes on brick construction: manufacturing of Brick. Brick Ind Assoc 1–7.
- Brooks, A.L., Zhou, H., Hanna, D., 2018. Comparative study of the mechanical and thermal properties of lightweight cementitious composites. Construct. Build. Mater. 159, 316–328. https://doi.org/10.1016/j.conbuildmat.2017.10.102.
- Brooks, A.L., Shen, Z., Zhou, H., 2020. Development of a high-temperature inorganic synthetic foam with recycled fly-ash cenospheres for thermal insulation brick manufacturing. J. Clean. Prod. 246, 118748 https://doi.org/10.1016/j. iclepro.2019.118748.
- Carlucci, S., 2013. Thermal Comfort Assessment of Buildings. Springer Milan Heidelberg, New York Dordrecht London. https://doi.org/10.1007/978-88-470-5238-3.
- Cuce, P.M., Riffat, S., 2016. A state of the art review of evaporative cooling systems for building applications. Renew. Sustain. Energy Rev. 54, 1240–1249. https://doi.org/ 10.1016/j.rser.2015.10.066.
- Cui, S., Ahn, C., Wingert, M.C., Leung, D., Cai, S., Chen, R., 2016. Bio-inspired effective and regenerable building cooling using tough hydrogels. Appl. Energy 168, 332–339. https://doi.org/10.1016/j.apenergy.2016.01.058.
- Edition, S.I., Erbe, D.H., Lane, M.D., Anderson, S.I., Baselici, P.A., Hanson, S., et al., 2013. ANSI/ASHRAE/IES Standard 90.1-2013 Energy Standard for Buildings except Low-Rise Residential Buildings (SI Edition), vol. 2013.

- Grupa, Tom, 2022. Brick Prices. Home Guid 2021. https://homeguide.com/costs/bri
- Haghighi, E., Or, D., 2013. Evaporation from porous surfaces into turbulent airflows: coupling eddy characteristics with pore scale vapor diffusion. Water Resour. Res. 49, 8432–8442. https://doi.org/10.1002/2012WR013324.
- He, Y., Zhang, Y., Zhang, C., Zhou, H., 2020. Energy-saving potential of 3D printed concrete building with integrated living wall. Energy Build. 222, 110110.
- ISO., 2005. ISO 7730: ergonomics of the thermal environment Analytical determination and interpretation of thermal comfort using calculation of the PMV and PPD indices and local thermal comfort criteria. Management 3, 605–615. https://doi.org/ 10.1016/j.soildvn.2004.11.005.
- Karamanis, D., 2015. Solar Cooling with Hydrophilic Porous Materials for Reducing Building Cooling Needs. Elsevier Ltd. https://doi.org/10.1016/B978-1-78242-380-5.00010-8
- ketan, Nayak A., Hagishima, A., Tanimoto, J., 2020. A simplified numerical model for evaporative cooling by water spray over roof surfaces. Appl. Therm. Eng. 165, 114514 https://doi.org/10.1016/j.applthermaleng.2019.114514.
- Kloppers, J.C., Kröger, D.G., 2005. The Lewis factor and its influence on the performance prediction of wet-cooling towers. Int. J. Therm. Sci. 44, 879–884. https://doi.org/ 10.1016/i.jithermalsci.2005.03.006.
- Kumar, N., Arakeri, J.H., 2019. Experimental and numerical investigation of evaporation from line sources of water in low porosity surfaces. J. Hydrol. 569, 795–808. https://doi.org/10.1016/j.jhydrol.2019.01.001.
- Kumar, R., Kaushik, S.C., 2005. Performance evaluation of green roof and shading for thermal protection of buildings. Build. Environ. 40, 1505–1511. https://doi.org/ 10.1016/j.buildenv.2004.11.015.
- Liang, X., Zhang, X., Liu, Z., Huang, Q., Zhang, H., Liu, C., et al., 2020. Direction-limited water transport and inhibited heat convection loss of gradient-structured hydrogels for highly efficient interfacial evaporation. Sol. Energy 201, 581–588. https://doi. org/10.1016/j.solener.2020.03.042.
- Liao, W., Zhuang, Y., Zeng, C., Deng, W., Huang, J., Ma, H., 2020. Fiber optic sensors enabled monitoring of thermal curling of concrete pavement slab: temperature, strain and inclination. Meas J Int Meas Confed 165, 108203. https://doi.org/ 10.1016/j.measurement.2020.108203.
- Liao, W., Zeng, C., Zhuang, Y., Ma, H., Deng, W., Huang, J., 2021. Mitigation of thermal curling of concrete slab using phase change material: a feasibility study. Cem. Concr. Compos. 120, 104021 https://doi.org/10.1016/j.cemconcomp.2021.104021.
- Martins, A.F., Bennett, N.C., Clavel, S., Groenewald, H., Hensman, S., Hoby, S., et al., 2018. Locally-curved geometry generates bending cracks in the African elephant skin. Nat. Commun. 9, 1–8. https://doi.org/10.1038/s41467-018-06257-3.
- Mehrangiz, Yazdanian, JHK, 1994. Measurement of the exterior convective film coefficient for windows in low-rise buildings. Build. Eng. 100, 1087–1096.
- Mosthaf, Klaus, Helmig, Rainer, Do, 2014. Modeling and analysis of evaporation processes from porous media on the REV scale. Water Resour. Res. 50, 5375–5377. https://doi.org/10.1002/2013WR014979.Reply.
- Nahar, N.M., Sharma, P., Purohit, M.M., 2003. Performance of different passive techniques for cooling of buildings in arid regions. Build. Environ. 38, 109–116. https://doi.org/10.1016/S0360-1323(02)00029-X.
- Palyvos, J.A., 2008. A survey of wind convection coefficient correlations for building envelope energy systems' modeling. Appl. Therm. Eng. 28, 801–808. https://doi. org/10.1016/j.applthermaleng.2007.12.005.
- Performance, M., Spectrophotom, N.I., Mass, A., Solar, Z., Tables, I., Materials, S., et al., 1996. Standard Test Method for Solar Absorptance, Reflectance, and Transmittance of Materials Using Integrating Spheres 1, pp. 1–9. https://doi.org/10.1520/E0903-20.2.03

- Poós, T., Varju, E., 2020. Mass transfer coefficient for water evaporation by theoretical and empirical correlations. Int. J. Heat Mass Tran. 153, 119500 https://doi.org/ 10.1016/j.ijheatmasstransfer.2020.119500.
- Prat, M., 2007. On the influence of pore shape, contact angle and film flows on drying of capillary porous media. Int. J. Heat Mass Tran. 50, 1455–1468. https://doi.org/ 10.1016/j.ijheatmasstransfer.2006.09.001.
- Rolph, G., Stein, A., Stunder, B., 2017. Real-time environmental applications and display sYstem: READY. Environ. Model. Software 95, 210–228. https://doi.org/10.1016/j. envsoft.2017.06.025.
- Rotzetter, A.C.C., Schumacher, C.M., Bubenhofer, S.B., Grass, R.N., Gerber, L.C., Zeltner, M., et al., 2012. Thermoresponsive polymer induced sweating surfaces as an efficient way to passively cool buildings. Adv. Mater. 24, 5352–5356. https://doi. org/10.1002/adma.201202574.
- Shafique, M., Kim, R., Rafiq, M., 2018. Green roof benefits, opportunities and challenges
   a review. Renew. Sustain. Energy Rev. 90, 757–773. https://doi.org/10.1016/j.
  rser 2018 04 006
- Shahraeeni, E., Or, D., 2012. Pore scale mechanisms for enhanced vapor transport through partially saturated porous media. Water Resour. Res. 48, 1–16. https://doi. org/10.1029/2011WR011036.
- Shahraeeni, E., Lehmann, P., Or, D., 2012. Coupling of evaporative fluxes from drying porous surfaces with air boundary layer: characteristics of evaporation from discrete pores. Water Resour. Res. 48, 1–15. https://doi.org/10.1029/2012WR011857.
- Sharifi, A., Yamagata, Y., 2015. Roof ponds as passive heating and cooling systems: a systematic review. Appl. Energy 160, 336–357. https://doi.org/10.1016/j. approxes. 2015.00.061
- Shokri, N., Or, D., 2011. What determines drying rates at the onset of diffusion controlled stage-2 evaporation from porous media? Water Resour. Res. 47, 1–8. https://doi. org/10.1029/2010WR010284.
- Shokri Kuehni, S.M.S., Bou-Zeid, E., Webb, C., Shokri, N., 2016. Roof cooling by direct evaporation from a porous layer. Energy Build. 127, 521–528. https://doi.org/ 10.1016/j.enbuild.2016.06.019.
- Spanaki, A., Tsoutsos, T., Kolokotsa, D., 2011. On the selection and design of the proper roof pond variant for passive cooling purposes. Renew. Sustain. Energy Rev. 15, 3523–3533. https://doi.org/10.1016/j.rser.2011.05.007.
- Thomas, W.C., DMB, 1990. Experimental validation of a mathematical model for predicting water vapor sorption at interior building surfaces. Build. Eng. 96, 487–496.
- Wanphen, S., Nagano, K., 2009. Experimental study of the performance of porous materials to moderate the roof surface temperature by its evaporative cooling effect. Build. Environ. 44, 338–351. https://doi.org/10.1016/j.buildenv.2008.03.012.
- Xu, X., Dessel, S Van, 2008. Evaluation of an active building envelope window-system. Build. Environ. 43, 1785–1791. https://doi.org/10.1016/j.buildenv.2007.10.013.
- Zhang, L., Zhang, R., Hong, T., Zhang, Y., Meng, Q., 2018. Impact of post-rainfall evaporation from porous roof tiles on building cooling load in subtropical China. Appl. Therm. Eng. 142, 391–400. https://doi.org/10.1016/j. applthermaleng.2018.07.033.
- Zhou, H., Brooks, A.L., 2019. Thermal and mechanical properties of structural lightweight concrete containing lightweight aggregates and fly-ash cenospheres. Construct. Build. Mater. 198, 512–526. https://doi.org/10.1016/j. conbuildmat 2018 11 074
- Zhou, T., Yang, J., Zhu, D., Zheng, J., Handschuh-Wang, S., Zhou, X., et al., 2017. Hydrophilic sponges for leaf-inspired continuous pumping of liquids. Adv. Sci. 4 https://doi.org/10.1002/advs.201700028.